Journal of Thermal Science Vol.32, No.3 (2023) 1049−1062

https://doi.org/10.1007/s11630-023-1791-1 **Article ID: 1003-2169(2023)03-1049-14**

Thermal and Structural Insight into Lightweight Lattice Channels for Active Cooling Technology

YANG Zenan[1], LUO Xiaobo[1], CHEN Wei[1*], JU Yinchao[2], ZHANG Bo[2]

1. School of Aeronautics and Astronautics, Sichuan University, Chengdu 610065, China
2. Beijing Power Machinery Institute, Beijing 100074, China

Abstract: The active cooling technology that can reduce the combustor temperature is commonly used to protect the scramjet. In order to further improve the performance of active cooling, the structural weight reduction, cooling efficiency and stress level of the cooling channel must be considered simultaneously. In this paper, new types of lattice channels for active cooling were designed and compared with the conventional cooling channel in terms of weight reduction, thermal and structural performance. The results showed that, at the same channel height, the cooling channel with staggered lattice arrays has the optimal comprehensive performance: the weight reduction effect reaches 39.93%; the wall temperature drops significantly, and the maximum *Nu* number is 2.155 times of the conventional channel. The flow field analysis showed that horseshoe vortices formed by the impact effect and hairpin vortices near the trailing edge are the main factors of heat transfer enhancement. The disturbed boundary layer and the excited turbulent kinetic energy also contribute much to enhance the heat transfer. In addition, due to the HTE-induced increment of metal tensile strength, the system reliability of lattice channel is better than the conventional one.

Keywords: active cooling, lattice channel, supercritical hydrocarbon fuel, enhanced heat transfer, structural analysis

1. Introduction

Hypersonic vehicle that pursues high performance brings extremely high thermal load to the scramjet [1], and the thermal stress generated by the non-uniform temperature distribution may cause the destruction of the combustor. The general thermal protection technology cannot meet the reliability requirements of the scramjet, so the active cooling technology must be introduced to keep the temperature of combustor within the allowable range of the combustor materials [2]. The hydrocarbon fuel is chosen as coolant, which avoids carrying extra coolant. In active cooling for hypersonic vehicles, as shown in Fig. 1, the hydrocarbon fuel firstly flows through the micro cooling channels around the combustor to remove the high heat load and then is injected into the combustor.

Therefore, the flow and heat transfer behaviors of supercritical hydrocarbon fuels which are used in active cooling technology need to be investigated. The heat transfer characteristics of JP-7 under conditions relevant to a Mach 8 propulsion system were experimentally studied by Linne [3]. The heat transfer deterioration occurred in the high heat flux condition and led to tube

Received: Jan 19, 2021 AE: YAN Suying Corresponding author: CHEN Wei E-mail: chenwei2017@scu.edu.cn

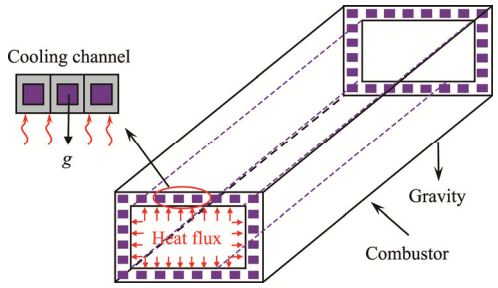

Fig. 1 Scramjet combustor and cooling channels

failure, and the carbon deposits was much higher than that in a low heat flux condition. Lei et al. [4] numerically studied the effects of mass flow rate, heat flux and hydraulic diameter on heat transfer and cracking of supercritical n-decane, and summarized empirical heat transfer correlations. Tao et al. [5] numerically analyzed the heat transfer and pyrolysis processes of supercritical pressure n-decane, and the influence mechanism of pyrolysis on heat transfer characteristics and flow resistance. It was discovered that the fluid acceleration plays the dominant role in heat transfer enhancement and brings more flow resistance. In Ref. [6], the effects of pressure, mass flow and heat flux on the supercritical n-decane heat transfer instability were experimentally studied. Turbulence transition and density fluctuation were considered to be the main causes. Zhang et al. [7] developed empirical correlations for heat transfer of supercritical n-decane. In his experiments, the pressure ranges from 4 MPa to 4.3 MPa, and the Reynolds number ranges from 800 to 70 000. Jiang et al. [8] analyzed the effects of rotation speed, operating pressure, mass flow rate and heat flux on the heat transfer performance of supercritical n-decane, and found that the centrifugation-induced buoyancy effect can prevent the occurrence of deteriorated heat transfer. Cheng [9] made numerical investigations of heat transfer performance of supercritical RP-3 kerosene in tubes with different diameters, and found that the increase in diameter led to a decrease in the heat transfer coefficient, which was suggested to be caused by the buoyancy effect. Yan [10] reported that the heat transfer performance of hydrocarbon fuel in horizontal mini tube was mainly affected by the thermo-physical properties and buoyance effect. The influence of hyper gravity on heat transfer characteristics of supercritical aviation kerosene in horizontal tube was studied by Lv [11]. It was concluded that the buoyancy effect caused by hyper gravity can amplify the temperature difference between the top and bottom walls. Wang et al. [12] explored the heat transfer deterioration and thermo-acoustic instability phenomena of supercritical aviation kerosene RP-3 in vertical tubes. It was believed that heat transfer deterioration was dominated by high buoyancy and thermal acceleration and thermo-acoustic instability was caused by pseudo-critical boiling effect. Li et al. [13] numerically studied the deteriorated heat transfer phenomenon of supercritical n-decane in vertical tubes and confirmed that heat transfer deteriorated (HTD) occurred when the fluid temperature in the buffer layer reached pseudo-critical temperature. In addition, many studies have also focused on the relationship between pressure oscillation and heat transfer in supercritical hydrocarbon fuels [14–19].

Considerable efforts have also been directed at enhancing the thermal performance of active cooling channels. Hitch [20] employed turbulating inserts, including twisted tape, louvered strip and static mixer, to enhance the heat transfer of supercritical hydrocarbon fuel. Results showed that all of the three types of turbulators can damp the pressure oscillation and heat transfer deterioration, and the greatest heat transfer enhancement was obtained with a static mixer. Li [21] employed micro-ribs to vanish the HTD phenomenon of supercritical n-decane flowing in rectangular mini-channels. Zhu [22] studied the heat transfer instability and oscillation characteristics of supercritical n-decane under different inlet temperature, pressure, mass flow rate and flow direction. The twisted stainless wire was used as the turbulator to eliminate the oscillation. It was found that the twisted wire inserted from the tube inlet can effectively suppress the oscillation. Ruan et al. [23] numerically studied the heat transfer performance of CuO-methane nanofluid at supercritical pressure, and found that the heat transfer enhancement was closely related to the density and turbulent viscosity variations in the buffer layer. Li [24] attributes the thermal performance improvement of supercritical n-decane in cooling channels with truncated ribs to the vortex-induced velocity and turbulence improvement.

However, the above structures increased the channel weight while enhancing the heat transfer, which had a negative influence on the thrust-to-weight ratio of the vehicle. Thus, the thermal performance of the cooling channel needs to be optimized without increasing the system weight. In recent years, additive manufacturing technology (3D printing) is increasingly mature, which provided the necessary conditions for the complicated cooling channels. Lattice structures are defined as those made up of an interconnected network of solid struts that form the edges and faces of cells [25]. Ref. [26] shows that, the heat transfer enhancement effect of lattice array is up to 3 times that of smooth channel. Moreover, the lattice structure that has excellent specific strength and stiffness can perfectly resist the plastic dynamic buckling under compression or shear load.

In view of the above points, a three-dimensional numerical model of supercritical n-decane flow inside

horizontal rectangular channel was built and validated. Based on this model, both the thermal performance of supercritical n-decane and stress properties of the lightweight lattice channels were numerically studied in this paper. This work can provide theoretical reference for the application of lattice arrays in active cooling technology.

2. Numerical Models

2.1 Physical models

A simplified model of the conventional active cooling channel was built to evaluate the thermal and structural performance of the lattice channels, and the model was shown in Fig. 2(a). This model consists of three smooth channels, which facilitates the subsequent lightweight structure design. The channel has the height of 1.5 mm, width of 2 mm, length of 60 mm. The wall thickness between the cooling channels is 1 mm, and the thickness of the upper and lower end walls is 1.5 mm. The thickness of top and bottom walls was reduced to contribute to the design of lightweight cooling channels. As shown in Fig. 3, three types of lattice channels were proposed in this study. In-line lattice arrays were adopted in Case 1 and Case 2, while staggered lattice arrays were adopted in Case 3. In Case 2 and Case 3, the barriers between cooling channels were removed for weight reduction. In addition, the channel height was increased to 2 mm, 2.5 mm and 3 mm for further weight reduction. Table 1 shows the detailed information of different lattice channels.

Fig. 4 shows the lattice channels with channel height of 2 mm, 2.5 mm and 3 mm, and Table 1 depicts the weight reduction ratios of different cooling channels. In comparison, the weight reduction ratio of Case 1 is relatively limited due to the barriers between adjacent channels. For Case 2 and Case 3, the weight decreases significantly after removing the barriers. In condition of the same channel height, the weight reduction ratio in Case 3 is smaller than that in Case 2 because the staggered lattice arrays have fewer lattices. The maximum weight reduction ratio occurs in Case 3_h2 with a value of 39.93%.

2.2 Boundary conditions

The solid zone (Inconel 718) and liquid zone (supercritical n-decane) are both considered due to the axial heat conduction of the material. The pressure at the outlet of the cooling channel is 4 MPa. The temperature of inlet coolant is set to 300 K, and the mass flow rate of each inlet is 0.04 kg/s. The bottom wall was uniformly heated by a heat flux of 3 MW/m^2. The sidewalls were symmetric boundary conditions, and the other walls were set at no-slip and adiabatic conditions. The thermophysical properties of supercritical n-decane, which were provided by chemical software Aspen HYSYS and thus shown in Fig. 5, were input into the CFD package Fluent by the method of piecewise-linear interpolation. This paper mainly focuses on the thermal and mechanical performance of lattice cooling channels; thus the pyrolysis process of the supercritical n-decane was not considered. In the structural analysis, the local model of the lattice position of fourth to sixth row of lattice units is taken as computing model. The two outer side walls of the cooling channel are symmetric constraints; the top wall of combustor is vertical constraint, and the bottom wall is fixed constraint. The mechanical properties of Inconel 718 were listed in Tables 2–5. The pressure in the combustion chamber was set at 0.15 MPa and the operating pressure in the cooling channel was set at 4 MPa.

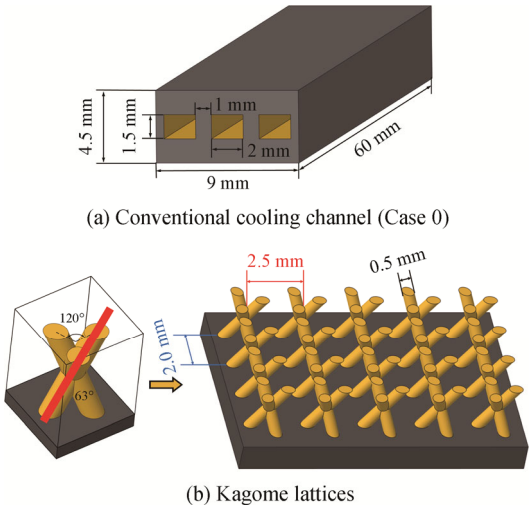

(a) Conventional cooling channel (Case 0)

(b) Kagome lattices

Fig. 2 Diagrams of conventional cooling channels and Kagome lattice array

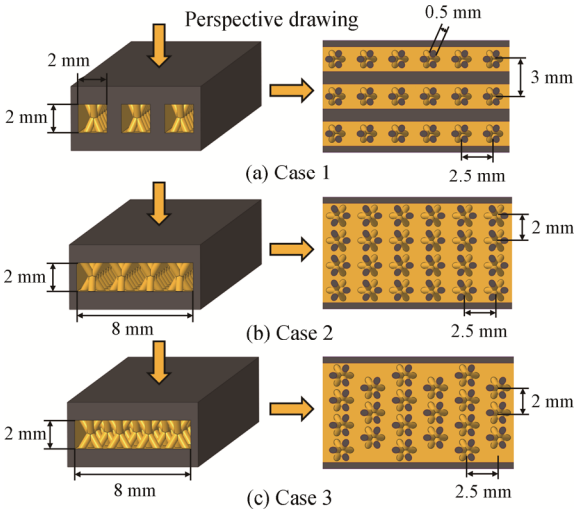

(a) Case 1

(b) Case 2

(c) Case 3

Fig. 3 Physical models for Case 1–Case 3

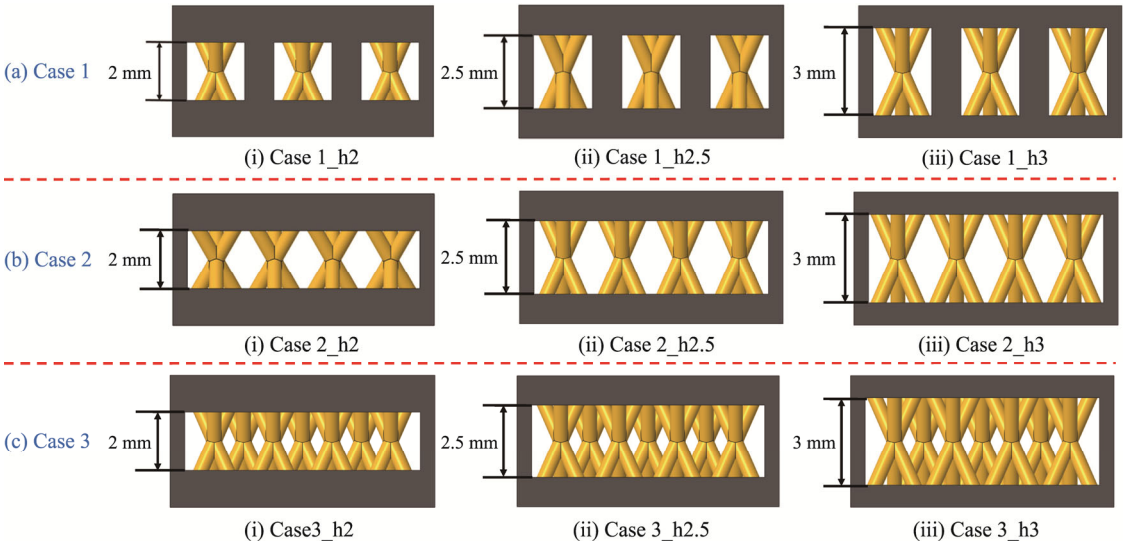

Fig. 4 Models for Case 1_h2–Case 3_h3

Table 1 Different lattice channels

Name	Introductions	Arrangement	Weight reduction ratio
Case 1_h2	Case 1, channel height 2 mm	–	5.62%
Case 1_h2.5	Case 1, channel height 2.5 mm	–	13.72%
Case 1_h3	Case 1, channel height 3 mm	–	22.08%
Case 2_h2	Case 2, channel height 2 mm	In-line	16.09%
Case 2_h2.5	Case 2, channel height 2.5 mm	In-line	27.81%
Case 2_h3	Case 2, channel height 3 mm	In-line	38.83%
Case 3_h2	Case 3, channel height 2 mm	Staggered	16.86%
Case 3_h2.5	Case 3, channel height 2.5 mm	Staggered	28.70%
Case 3_h3	Case 3, channel height 3 mm	Staggered	39.93%

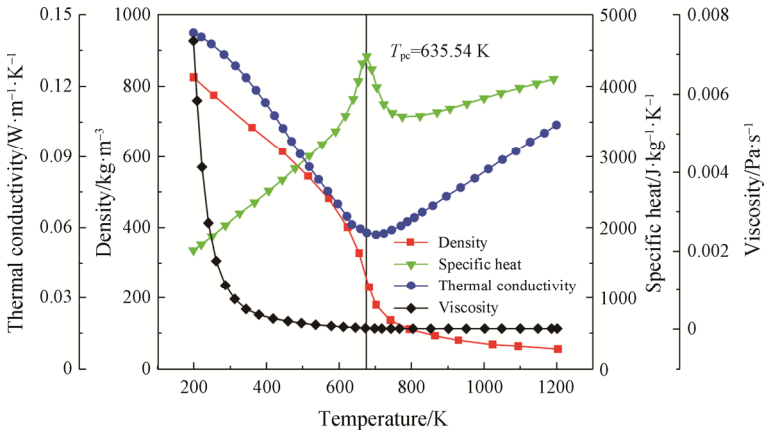

Fig. 5 Physical properties of n-decane at supercritical pressure (4 MPa)

Table 2 Elastic modulus E and Poisson's ratio v

T/K	293–493	673	773	873	923	973
E/GPa	204	176	160	150	146	141
v	0.3	0.3	0.3	0.3	0.3	0.33

Table 3 Coefficient of linear expansion

T/K	293–373	293–573	293–673	293–773	293–873	293–973	293–1073
$\alpha/10^{-6}$ K^{-1}	11.8	13.5	14.1	14.4	14.8	15.4	17

Table 4 Thermal conductivity

T/K	373	473	573	673	773	873	973	1073
λ/ W·(m·K)$^{-1}$	14.7	15.9	17.8	18.3	19.6	21.2	22.8	23.6

Table 5 Tensile strength σ_b

T/K	294	773	923
σ_b/MPa	1280	1130	1000

2.3 Numerical schemes

Ansys Fluent and Ansys Mechanical were adopted for flow and structural analysis, respectively. The mapping and node interpolation method was used to transmit thermal parameters of the fluid-solid interface to the structural analysis.

In the flow analysis, finite volume method is adopted to solve the steady Navier-Stokes equations, and the governing equations for mass, momentum and energy are as follows.

Continuity equation:

$$\frac{\partial(\rho u_i)}{\partial x_i}=0 \tag{1}$$

Momentum equation:

$$\frac{\partial(\rho u_i)}{\partial t}+\frac{\partial(\rho u_i u_j)}{\partial x_j} =-\frac{p}{x_i}+\frac{\partial}{\partial x_j}\left[\mu\frac{\partial(u_i)}{\partial x_j}-\rho u_i' u_j'\right]+\rho g \tag{2}$$

Energy equation:

$$\frac{\partial}{\partial x_i}(\rho T)+\frac{\partial}{\partial x_i}(\rho u_i T)=\frac{\partial}{\partial x_i}\left[\frac{\lambda}{c_p}\frac{\partial T}{\partial x_i}\right] \tag{3}$$

The standard k-ε turbulence model was proved to yield reliable results for supercritical n-decane flows in Section 2.5. The transport equations of k and ε are given as

$$\frac{\partial kU_j}{\partial x_j}=\frac{\partial}{\partial x_j}\left[\left(v+\frac{v_i}{\sigma_k}\right)\frac{\partial k}{\partial x_j}\right]+P_k-\varepsilon \tag{4}$$

$$\frac{\partial \varepsilon U_j}{\partial x_j}=\frac{\partial}{\partial x_j}\left[\left(v+\frac{v_i}{\sigma_\varepsilon}\right)\frac{\partial k}{\partial x_j}\right]+c_{\varepsilon 1}P_k\frac{\varepsilon}{k}-c_{\varepsilon 2}\frac{\varepsilon^2}{k} \tag{5}$$

where σ_k=1.0, σ_ε=1.3, $\sigma_{\varepsilon 1}$=1.35, $\sigma_{\varepsilon 2}$=1.80, and the turbulence production term $P_k=-\overline{u_i'u_i'}\frac{\partial U_i}{\partial x_j}$.

The constitutive equation is given as:

$$\varepsilon_{ij}=\frac{1}{2}\left(\eta_{i,j}+\eta_{j,i}\right)+\alpha\Delta T\delta_{ij} \tag{6}$$

The stress tensor σ_{ij} is as follows:

$$\sigma_{ij}=2G\varepsilon_{ij}+\lambda\Theta\delta_{ij} \tag{7}$$

The shear modulus G is given by:

$$G=\frac{E}{2(1+\upsilon)} \tag{8}$$

And the Lamé constant λ is defined by:

$$\lambda=\frac{\upsilon E}{(1+\upsilon)(1-2\upsilon)} \tag{9}$$

where E is Young's modulus, and υ is Poisson's ratio.

2.4 Grid independence test

As illustrated in Fig. 6, tetrahedral cells were adopted to construct the grids of computational domains. In the near-wall zone, 16 layers of prism cells were constructed with the first layer height of 1×10^{-6} m and height ratio of 1.1, which can meet the requirements of enhanced wall function.

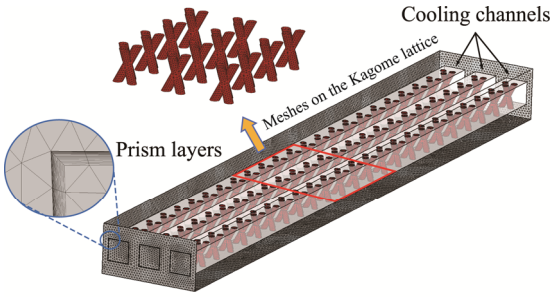

(a) Grid of cooling channel model

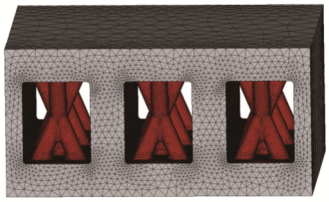

(b) Grid of structural analysis

Fig. 6 Grid of cooling channel model

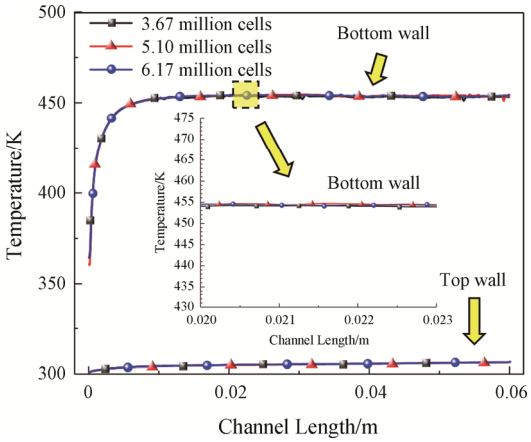

Fig. 7 Grid independence test

The grid independence test of Case 0 was carried out, with the grid number of 3.67 million, 5.10 million and 6.17 million, respectively. The inner wall temperature

distributions were shown in Fig. 7. It is concluded that the increase of mesh elements will not further change the wall temperature when grid number reaches 5.10 million. Thus, the grid of 5.10 million cells is adopted to balance the computational cost and numerical precision.

2.5 Validation of turbulence model

The numerical accuracy of standard k-ε, k-ω SST, transition SST turbulence models were compared based on the experimental data from Ref. [7]. As shown in Fig. 8, the mass flow rate m, wall heat flux q, inlet pressure P and inlet temperature T of the experiment are 1.24 g/s, 0.244 MW/m^2, 4 MPa and 297 K, respectively. From the wall temperature distribution of different numerical methods, it can be found that the minimum prediction deviation was obtained by the standard k-ε turbulence model. Although there exist some deviations, the trend of temperature variation can be captured obviously.

In Fig. 9, Zhao's experimental and numerical results [27, 28] were chosen for further validation. The operating conditions are listed as: the mass flow rate m, wall heat flux q, inlet pressure P and inlet temperature T of the experiment are 1.24 g/s, 0.4187 MW/m^2, 4 MPa and 297 K, respectively. It was found that standard k-ε turbulence model accurately captured the heat transfer characteristics of supercritical n-decane. The deviation between the local wall temperature and experimental data was due to the fact that the wall heat flux in the experiment was non-uniform. Based on the above discussions, it can be concluded that standard k-ε turbulence model is acceptable for the numerical simulations in this paper.

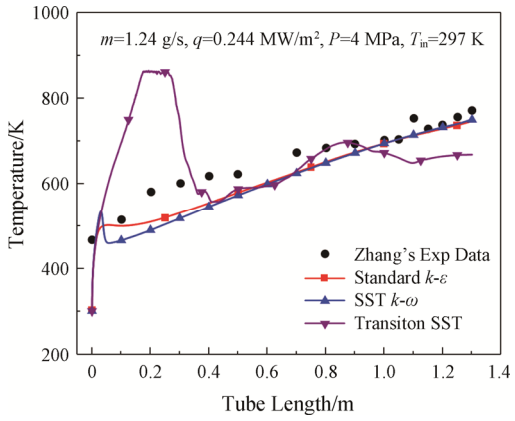

Fig. 8 Comparison between different turbulence models

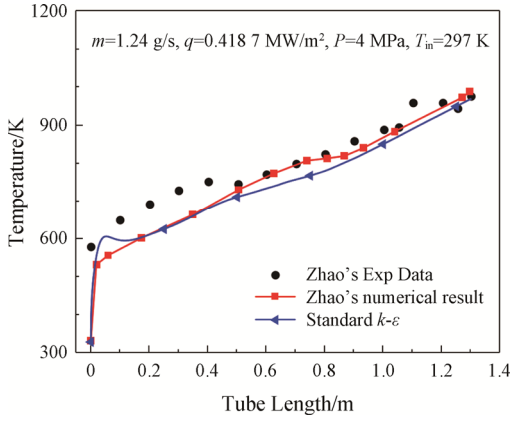

Fig. 9 Comparison between Zhao's experimental data and numerical results

3. Results and Discussion

3.1 Thermal performance

Fig. 10 illustrates the Y-Z plane average temperature distributions of the metal structures along the flow direction. It is observed that the average temperature of the solid structure decreases significantly with the increase of channel height. This suggests that the increase of channel height enhances the heat removal capacity of supercritical n-decane, and thus the bulk fluid can take away more heat through convective heat transfer. Comparatively speaking, the average wall temperature of Case 1 is the lowest. This is due to its heaviest wall structure weight as well as the higher thermal conductivity of the metal material. However, the structure of Case 1 will bring greater weight burden to the vehicle and lead to lower thrust-weight ratio. Compared with Case 2, Case 3 has a lower average temperature distribution due to the excellent heat transfer enhancement performance of the staggered lattice arrays.

The Nusselt number Nu is defined by:

$$Nu = hd/\lambda \tag{10}$$

The convective heat transfer coefficient h is:

$$h = \frac{q}{T_w - T_b} \tag{11}$$

where T_w is inner wall temperature and T_b is bulk fluid temperature.

The local Nu number distributions on the endwalls of Case 0–Case 3 are depicted in Fig. 11. Compared with the smooth channel, the Nu number at the leading and trailing edges of the lattices in Case 1 significantly increased. At the same time, the heat transfer in the wake zone was activated due to the vortical flows. Thus, the overall thermal performance of lattice channel was improved. The average heat transfer on the endwall further increased with the increase of channel height, which was due to the further developing vortical flow. Furthermore, the convective heat transfer in the channel without barriers was significantly stronger than that of Case 1. This suggests that the heat conduction effect of metal barriers as well as the incompact lattice arrangement in Case 1 hindered the convective heat transfer.

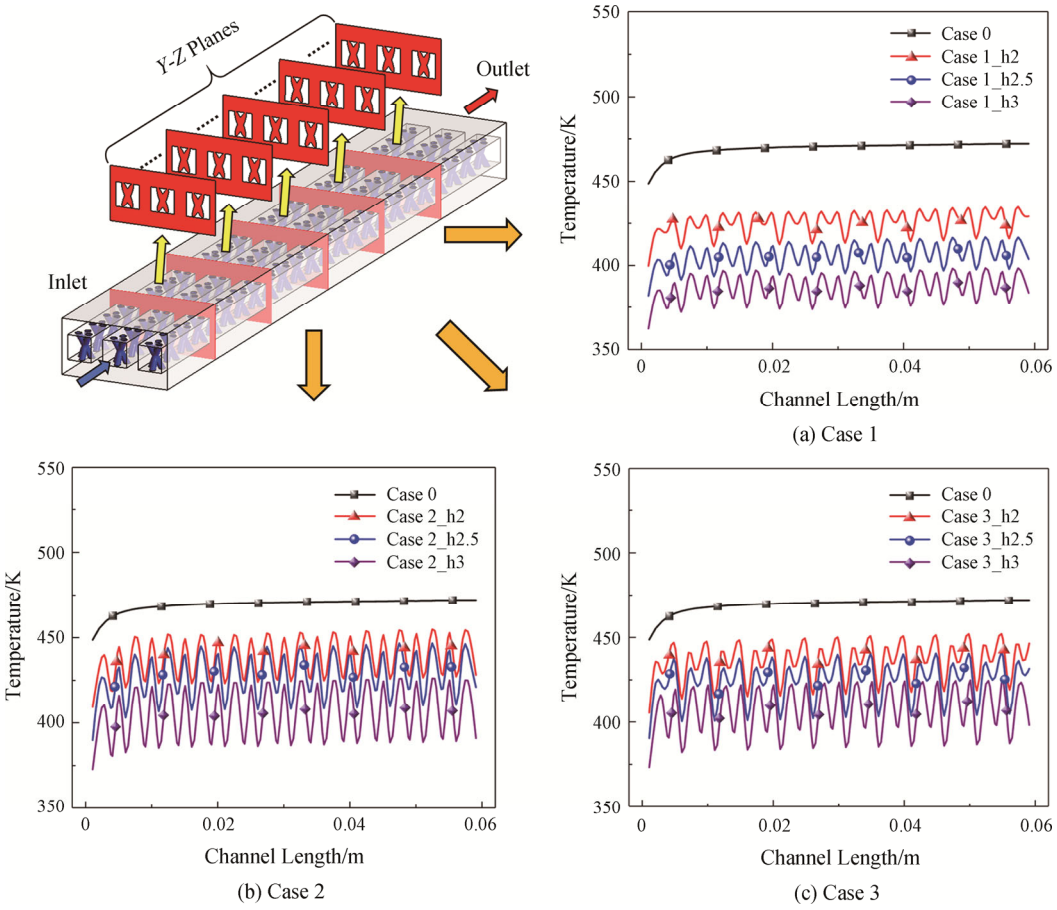

Fig. 10 Average temperature distributions of the structures along the flow direction

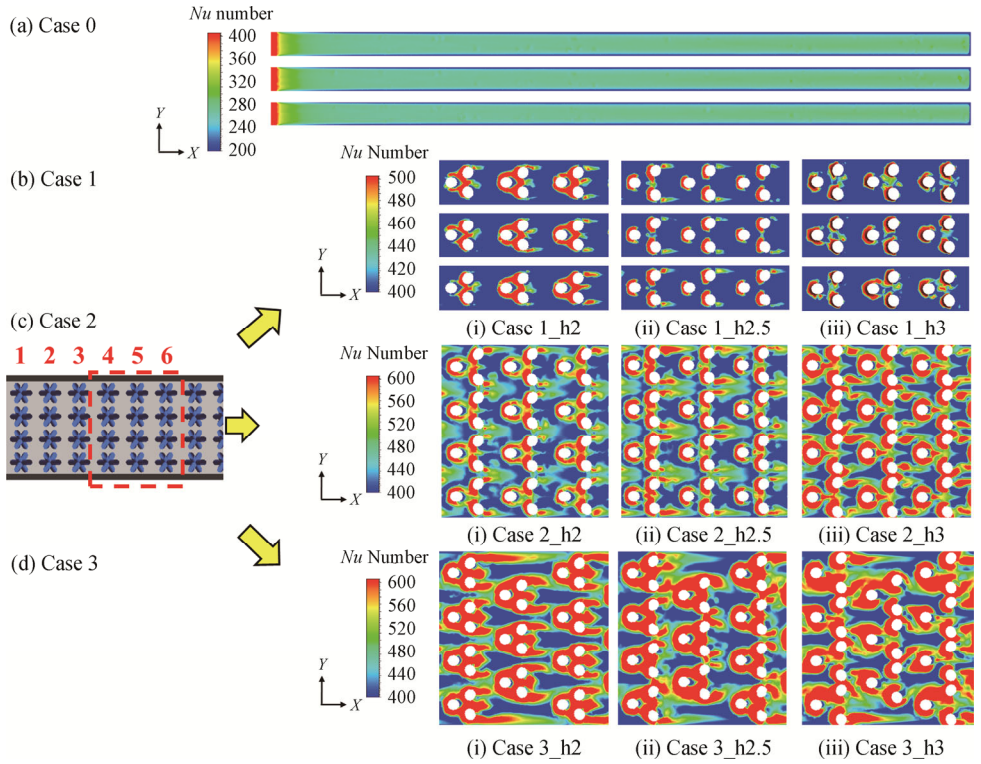

Fig. 11 Contours of *Nu* number distributions on the bottom walls of Case 0–Case 3

Fig. 12 presents the Nu/Nu_0 of Case 1–Case 3, where Nu_0 equals to 266.0. Obviously, the heat transfer efficiency of Case 3 channel is the highest at the same height, followed by Case 2 and Case 1. This conforms to the heat transfer law of heat exchanger; that is, the thermal performance of the channel with staggered ribs is superior to the channel with in-line ribs. As the channel height increases, the heat transfer efficiency of the channel increases.

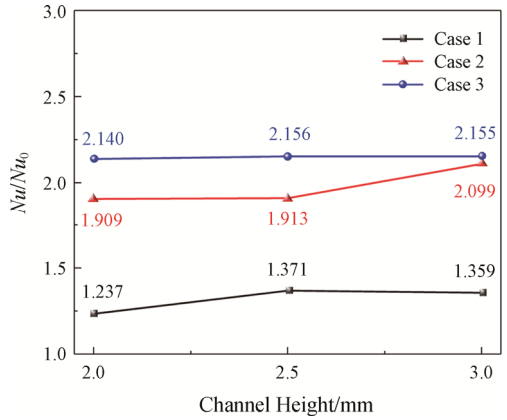

Fig. 12 The average Nu/Nu_0 vs. channel height

Fig. 13(a) provides the area-averaged Nu/Nu_0 on the struts of lattice arrays to characterize the contribution of lattice units to the convective heat transfer. With the increase of channel height, the heat transfer ability of the lattice arrays presents an increasing trend. Compared with the bottom wall, the average Nu number on the lattice surface is relatively higher due to the impact effect of upstream flow. Fig. 13(b) shows the heat flux ratio of the lattice surface to bottom wall Q'/Q as a function of the channel height. It is found that, the heat flux ratio of the lattice surface presents a monotonously increasing trend with the increase of channel height, and the highest ratio occurs in Case 2_h3 with a value of 27.87%. This is because that the lattice surface area is smaller than that of the bottom wall, and the temperature difference between the bulk fluid.

3.2 Heat transfer enhancement mechanism

In order to realize the detailed flow field characteristics inside the lattice channel, Fig. 14 provides the two-dimensional streamlines at the spanwise plane of X=0.025 m. It is found that vortical structures are generated by the Kagome lattice. The Kagome lattice shrinks the cross-sectional area, which increases the fluid velocity between lattice struts and subsequently enhances the local convective heat transfer. For Case 1 and Case 2, a counter-rotating vortex pair (CRVP) and corner vortices are generated. With the increase of channel height, corner vortices gradually evolve into another streamwise vortex pair above the original CRVP, further disturbing the flow field in the near-wall zone. Thus, the evolution of vortical structure further enhances the overall heat transfer as the channel height increases. For Case 3, the vortical structure is chaotic due to the existence of the staggered Kagome lattice arrays. However, there is still a strong secondary flow distribution between the endwall and the bulk fluid, which aggravates the convective mixing of hot and cold fluids. The vortex structure in the flow field can fully mix the bulk fluid with the thermal fluid in the boundary layer. The down-wash effect of vortex can also reduce the thermal boundary layer thickness.

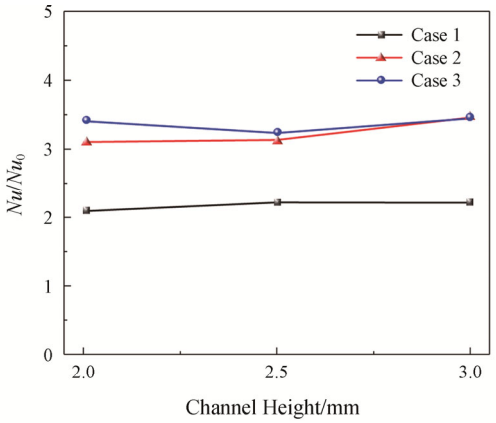

(a) Average Nu/Nu_0 on the lattice surface vs. channel height

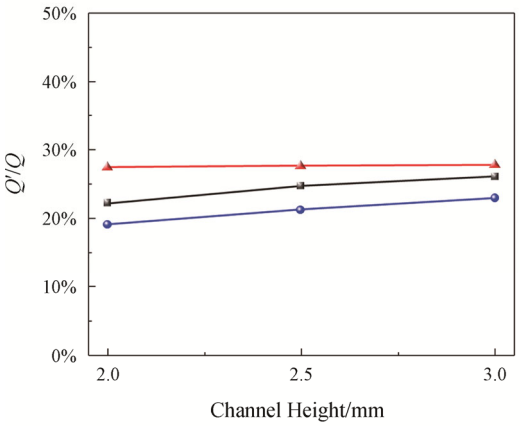

(b) Heat flux Q'/Q vs. channel height

Fig. 13 Average Nu/Nu_0 on the lattice surface and heat flux vs. channel height

Fig. 15 shows the streamline distribution on the X-Y planes for Case 1–Case 3. The jet-impingement effect of the upstream flow forms a horseshoe vortex structure at the leading edge of the Kagome lattice and greatly enhances local heat transfer. Near the trailing edge of lattice, the hairpin vortices form long wake zones and participate in the blending process between the mainstream and near-wall fluid.

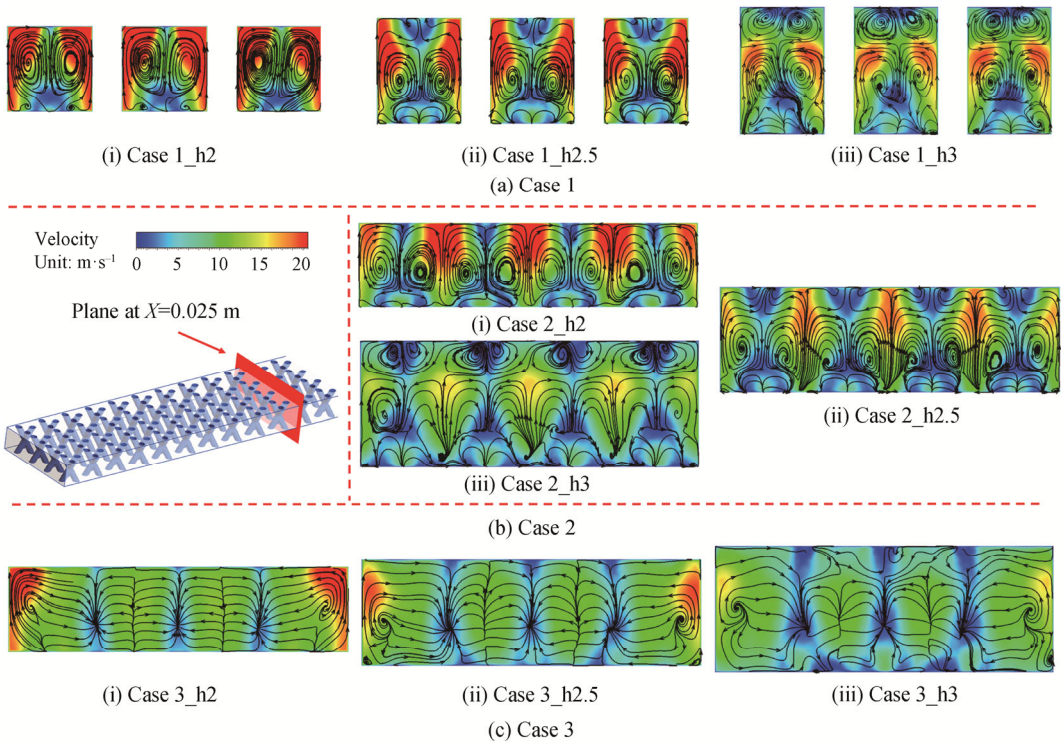

Fig. 14 Two-dimensional streamlines on the *Y*-*Z* planes at *X*=0.025 m

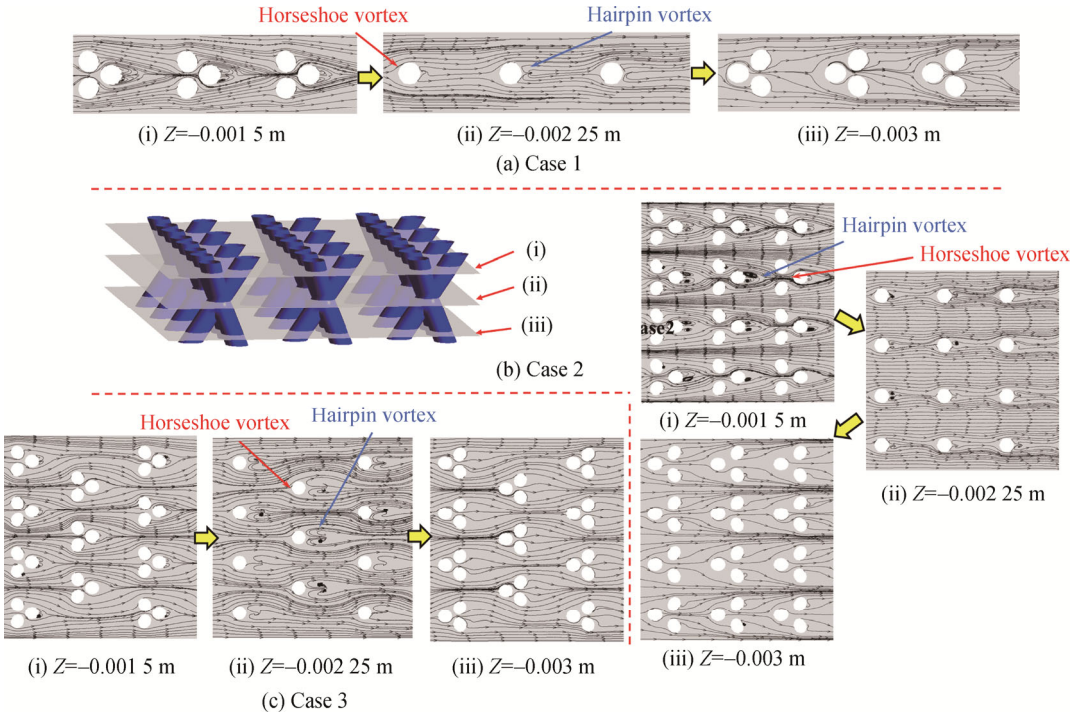

Fig. 15 Two-dimensional streamlines on the *X*-*Y* planes

Fig. 16 shows the streamlines and velocity distribution on the *X*-*Z* planes for Case 0_h2 to Case 3_h2. It is observed that the flow direction deflected at the trailing edge of the lattice unit and a standing vortex is generated near the bottom wall, which effectively intensifies the energy transport.

Fig. 17 compares the turbulent kinetic energy distribution at *X*=0.0075 m for Case 0–Case 3_h2. Compared with the smooth channel, the lattice in Case 1–Case 3 significantly improves the distribution of turbulent kinetic energy in the mainstream and boundary layer, effectively intensifies the turbulent energy

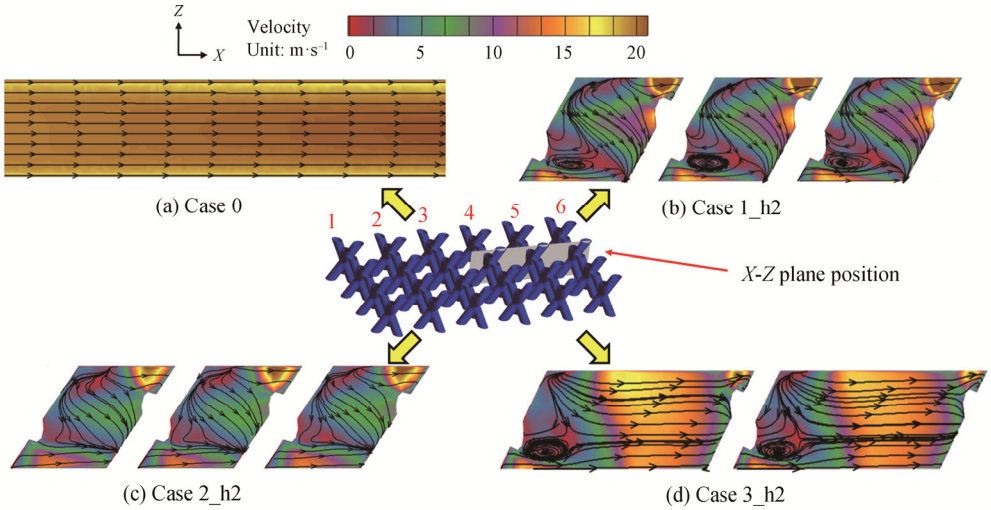

Fig. 16 Streamlines on the *X*-*Z* planes

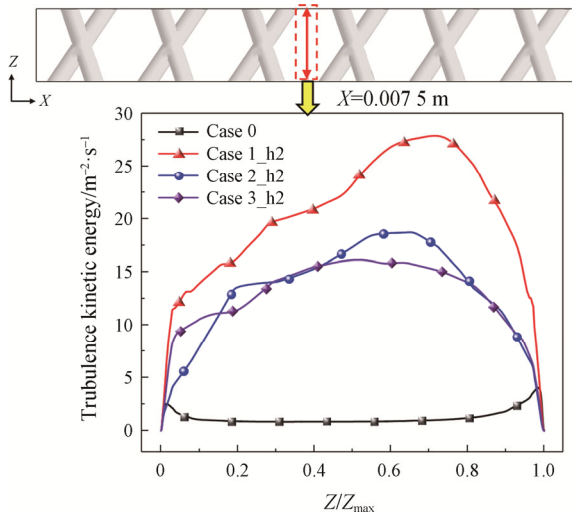

Fig. 17 Turbulent kinetic energy distributions at the trailing edge of the third row of lattice arrays

transport, and enhances the fluid heat transfer capacity. Therefore, the enhancement of turbulent kinetic energy distribution is also an important factor for the heat transfer enhancement in lattice channel. As the channel of Case 1 is relatively narrow, its large velocity and velocity gradient lead to the largest the turbulent kinetic energy distribution. The turbulent kinetic energy distribution in Case 2 and Case 3 is similar, and the turbulent kinetic energy in Case 2 is slightly stronger than Case 3 due to its larger number of lattice units.

3.3 Structural analysis

3.3.1 Stress analysis

The reduced thickness of the baffle and sidewall of the cooling channel undoubtedly affects the mechanical properties of the channel. Therefore, this section conducts strength checking for the structural stress and safety factor of the lattice channels.

Fig. 18 presents the contours of von-Mises stress for Case 0–Case 3, and the positions of maximum Mises stress were labeled as σ_{max}. For Case 0, the position of maximum Mises stress is on the heated wall. For Case 1–Case 3, the maximum values of Mises stress were all found at the rounded corners between the lattice arrays and the bottom wall of channel, which can be ascribed to the stress concentration. Compared with Case 0, the Mises stress on the heated wall of Case 1–Case 3 decreased significantly as well as the whole lattice channel, which indicated that the lattice structure effectively reduced the thermal stress. However, due to the reduction of channel weight, the Mises stress on the bottom wall of the lattice channels increased. With the increase of channel height, the overall Mises stress of the lattice channel decreases, ranging from 950 MPa to 1170 MPa. The Mises stress on the surfaces far from the position of stress concentration was approximately below 700 MPa.

Fig. 19 shows the maximum von-Mises stress σ_{max} for Case 0–Case 3. It was found that after installing the lattice arrays, the σ_{max} increased. With the increase of channel height, σ_{max} decreases monotonously. At the same channel height, the σ_{max} of Case 3 is the largest, followed by Case 2, and Case 1 is the smallest.

3.3.2 Safety factor analysis

The tensile strength is the critical value of metal transiting from uniform plastic deformation to local concentrated plastic deformation. It is also the maximum bearing capacity of metal under static tensile condition. In order to meet the design requirements, the local equivalent Mises stress should be smaller than the tensile strength. Safety factor is defined as the ratio of tensile strength σ_b (see Table 5) to the local von-Mises stress. With the value of safety factor greater than 1, the local Mises stress of lattice channel was lower than the tensile

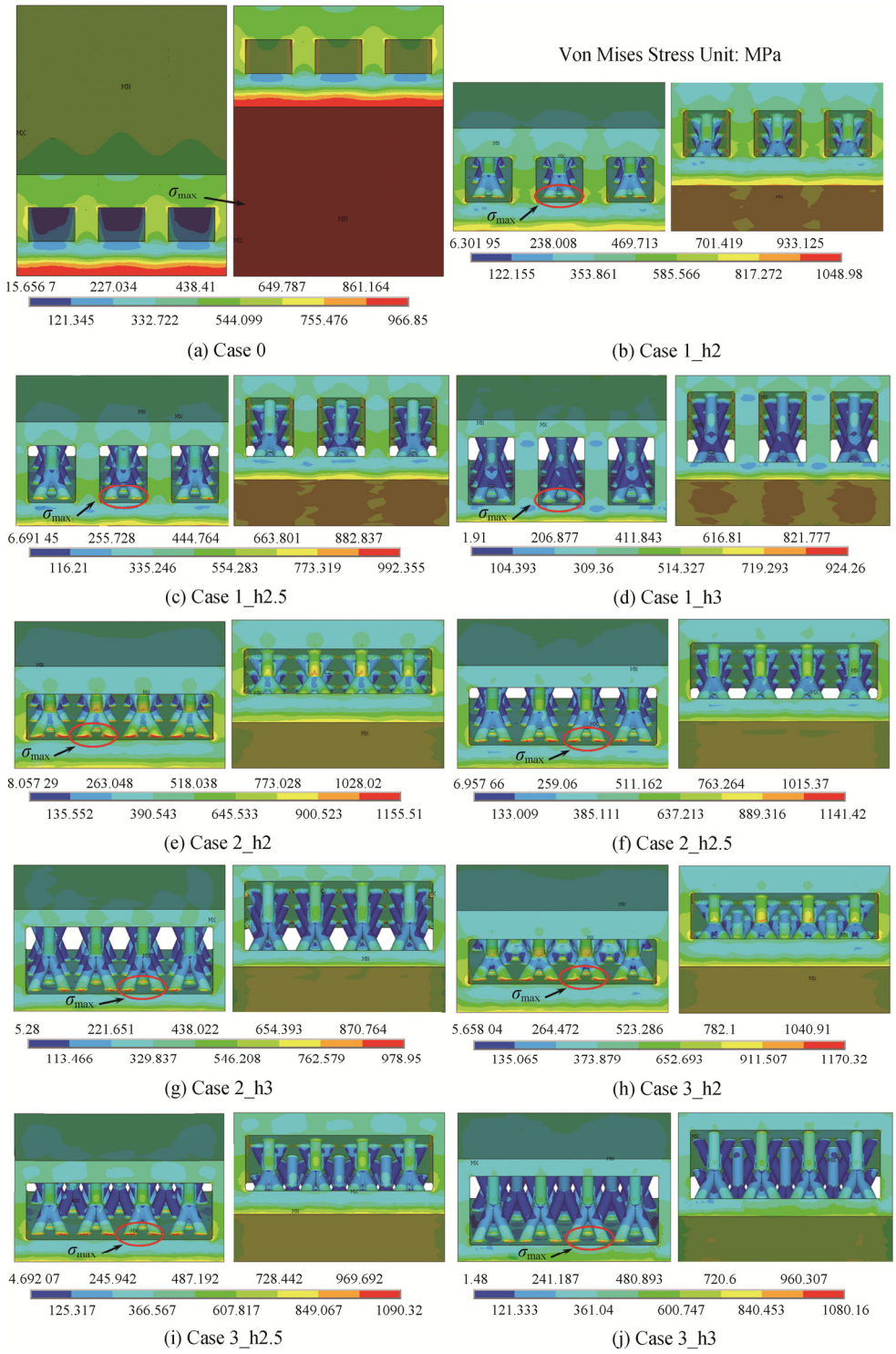

Fig. 18 The contours of von-Mises stress for Case0-Case3

strength under the combined effects of thermal and pressure loads. Conversely, it indicates that the local Mises stress is higher than the tensile strength.

Fig. 20(a) shows the minimum safety coefficient of equivalent Mises stress based on material tensile strength and the range of safety factors on the inner and outer walls of each scheme. The minimum value of safety factor was greater than 1 for each channel. The minimum safety factor occurred in Case 3_h2 and its value is 1.06, while the safety factors of the other channels are all greater than 1.06. In Case 1–Case 3, the tensile-strength-based safety factor increased with the increase of

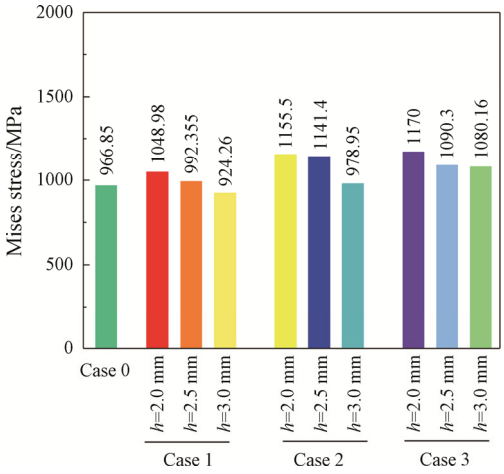

Fig. 19 The maximum von-Mises stress σ_{max} for Case 0–Case 3

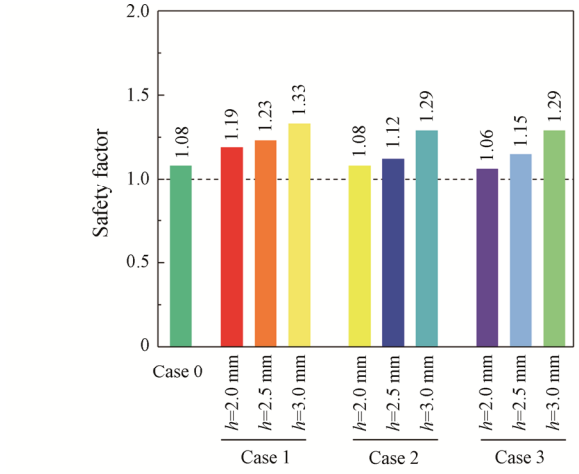

(a) Minimum safety factors for Case 0–Case 3

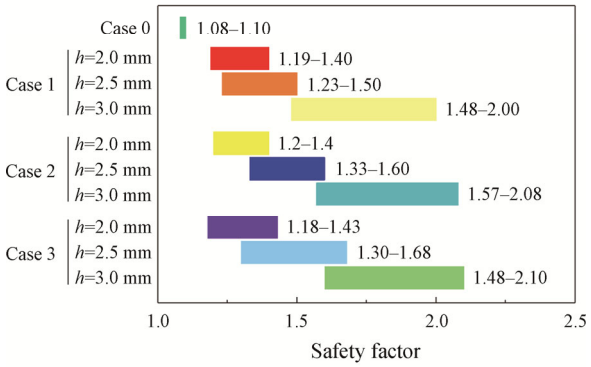

(b) Safety factors on the heated combustor wall

Fig. 20 Safety factors for Cases 0–3

channel height. When the channel height is 3 mm, the minimum safety factor for Case 1–Case 3 reaches 1.33, 1.29 and 1.29, respectively. The suggests that when the wall thickness is reduced, the heat transfer is enhanced and the wall temperature drops, which leads to the increase of material tensile strength and thus the increase of the safety factor. Fig. 20(b) shows the range of safety factor on the heated wall of channel. With the increase of channel height, the safety factor on the heated wall increases gradually. The safety factor on the heated wall of Case 0 ranges from 1.08 to 1.15. When the channel height reaches 3 mm, the minimum safety factor on the heated wall of Case 1–Case 3 reaches 1.48, 1.57 and 1.6, respectively, and the maximum safety coefficient reaches 2, 2.08 and 2.1, respectively.

4. Conclusions

In this paper, thermal and structural performance of active cooling in lattice channels is numerically studied. The effects of channel height and lattice arrangement on heat transfer and stress characteristics are investigated in detail. The main conclusions are drawn as follows:

(1) At the same channel height, Case 3 is the optimal choice for weight reduction, followed by Case 2, and Case 1 is the worst. The weight reduction ratio of Case 3_h3 can be as high as 39.93%.

(2) With the increase of channel height, the wall temperature of Case 1–Case 3 decreases monotonously, and the average *Nu* number increases. The average *Nu* number of Case 3_h2.5 is 2.156 times as high as that of the smooth channel. The heat flux on the lattice structure is about 20%–30% of that on the bottom wall, indicating that the lattice structure plays an important role in heat transfer enhancement.

(3) The jet-impingement effect of the upstream flow forms a horseshoe vortex structure at the leading edge of the Kagome lattice and greatly enhances local heat transfer. Near the trailing edge of lattice, the hairpin vortices form long wake zones and participate in the blending process between the mainstream and near-wall fluid. These are the main reasons of heat transfer enhancement. The disturbance of turbulent boundary layer and intensification of turbulent kinetic energy are also important factors to enhance heat transfer.

(4) The maximum stress of conventional channel appears at the heated wall, and the maximum stress of lattice channel is at the rounded corner between lattice and bottom wall. The stress decreases with the increase of channel height. The tensile-strength-based safety factor indicates that the structural stress of Case 0–Case 3 is within the allowable range. The lattice channel reduces the temperature of the structure due to the enhancement of heat transfer, which increases the tensile strength of metal and thus increases the safety factor of the structure.

(5) In terms of weight reduction, heat transfer and structural performance, the channel named Case 3_h3 is the optimal choice.

Acknowledgement

This research was supported by the National Natural Science Foundation of China (51876132) and the Science and Technology on Scramjet Laboratory (6142703190101).

References

[1] Xie J., Zhang R., Xie G., Manca O., Thermal and thermomechanical performance of actively cooled pyramidal sandwich panels. International Journal of Thermal Sciences, 2019, 139: 118–128.

[2] Zhong F., Fan X., Yu G., Li J., Sung C.J., Heat transfer of aviation kerosene at supercritical conditions. Journal of Thermophysics and Heat Transfer, 2009, 23(3): 543–550.

[3] Linne D., Meyer M., Edwards T., Eitman D., Evaluation of heat transfer and thermal stability of supercritical JP-7 fuel. 33rd Joint Propulsion Conference and Exhibit, 1997.

[4] Lei Z., He K., Huang Q., Bao Z., Li X., Numerical study on supercritical heat transfer of n-decane during pyrolysis in rectangular tubes. Applied Thermal Engineering, 2020, 170: 115002.

[5] Tao Z., Hu X., Zhu J., Wu H., Numerical investigation of pyrolysis effects on heat transfer characteristics and flow resistance of n-decane under supercritical pressure. Chinese Journal of Aeronautics, 2018, 31(6): 1249–1257.

[6] Yan J., Zhu Y., Zhao R., Yan S., Jiang P., Experimental investigation of the flow and heat transfer instabilities in n-decane at supercritical pressures in a vertical tube. International Journal of Heat and Mass Transfer, 2018, 120: 987–996.

[7] Zhang L., Zhang R.L., Xiao S.D., Jiang J., Le J.L., Experimental investigation on heat transfer correlations of n-decane under supercritical pressure. International Journal of Heat and Mass Transfer, 2013, 64: 393–400.

[8] Jiang P., Lu Z., Guo Y., Zhu Y., Experimental investigation of convective heat transfer of hydrocarbon fuels at supercritical pressures within rotating centrifugal channel. Applied Thermal Engineering, 2019, 147: 101–112.

[9] Cheng Z., Tao Z., Zhu J., Wu H., Diameter effect on the heat transfer of supercritical hydrocarbon fuel in horizontal tubes under turbulent conditions. Applied Thermal Engineering, 2018, 134: 39–53.

[10] Yan J., Liu S., Guo P., Bai C., Experimental investigation on convection heat transfer of supercritical hydrocarbon fuel in a long mini tube. Experimental Thermal and Fluid Science, 2020, 115: 110100.

[11] Lv L., Wen J., Fu Y., Quan Y., Zhu J., Xu G., Numerical investigation on convective heat transfer of supercritical aviation kerosene in a horizontal tube under hyper gravity conditions. Aerospace Science and Technology, 2020, 105: 105962.

[12] Wang Y., Li S., Dong M., Experimental investigation on heat transfer deterioration and thermo-acoustic instability of supercritical-pressure aviation kerosene within a vertical upward circular tube. Applied Thermal Engineering, 2019, 157: 113707.

[13] Li Y., Sun F., Xie G., Sundén B., Numerical analysis of supercritical n-decane upward flow and heat transfer characteristics in the buffer layer of a vertical tube. Numerical Heat Transfer, Part A: Applications, 2019, 77(3): 247–265.

[14] Hines W.S., Pressure oscillations associated with heat transfer to hydrocarbon fluids at supercritical pressures and temperatures. Physics, 1962, 32(3): 361–366.

[15] Hunt S.A., Thermoacoustic oscillations of jet-A fuel in parallel heated flowpaths. ASME 2015 International Mechanical Engineering Congress and Exposition. American Society of Mechanical Engineers, 2015.

[16] Hunt S., Heister S.D., Thermoacoustic oscillations in supercritical fuel flows. 12th International Energy Conversion Engineering Conference, 2014.

[17] Linne D., Meyer M., Braun D., Keller D., Investigation of instabilities and heat transfer phenomena in supercritical fuels at high heat flux and temperatures. 36th AIAA/ASME/SAE/ASEE Joint Propulsion Conference and Exhibit, 2000.

[18] Barber J., Brutin D., Sefiane K., Gardarein J.L., Tadrist L., Unsteady-state fluctuations analysis during bubble growth in a “rectangular” microchannel. International Journal of Heat and Mass Transfer, 2011, 54(23–24): 4784–4795.

[19] Stiegemeier B., Meyer M., Taghavi R., A thermal stability and heat transfer investigation of five hydrocarbon fuels. 38th AIAA/ASME/SAE/ASEE Joint Propulsion Conference & Exhibit, 2002.

[20] Hitch B., Karpuk M., Enhancement of heat transfer and elimination of flow oscillations in supercritical fuels. 34th AIAA/ASME/SAE/ASEE Joint Propulsion Conference and Exhibit, 1998.

[21] Li X., Zhang S., Qin J., Bao W., Parametric analysis on the thermal behavior of cracking hydrocarbon fuel flow inside asymmetry heated cooling channels with micro-ribs. International Journal of Heat and Mass Transfer, 2020, 160: 120154.

[22] Zhu Y., Zhao R., Wang Y., Jiang P.X., Investigation of flow and heat transfer instabilities and oscillation inhibition of n-decane at supercritical pressure in vertical pipe. Applied Thermal Engineering, 2019, 161: 114143.

[23] Ruan B., Gao X., Meng H., Numerical modeling of turbulent heat transfer of a nanofluid at supercritical pressure. Applied Thermal Engineering, 2017, 113:

994–1003.

[24] Li Y., Sun F., Xie G., Qin J., Improved thermal performance of cooling channels with truncated ribs for a scramjet combustor fueled by endothermic hydrocarbon. Applied Thermal Engineering, 2018, 142: 695–708.

[25] Lu T.J., Xu F., Wen T., Thermo-fluid behavior of periodic cellular metals. Science Press, 2013.

[26] Liang D., Bai W., Chen W., Investigating the effect of element shape of the face-centered cubic lattice structure on the flow and endwall heat transfer characteristics in a rectangular channel. International Journal of Heat and Mass Transfer, 2020, 153: 119579.

[27] Zhao G., Song W., Zhang R., Effect of pressure on thermal cracking of china RP-3 aviation kerosene under supercritical conditions. International Journal of Heat and Mass Transfer, 2015, 84: 625–632.

[28] Zhao G., Song W., Zhang R., Three-dimensional numerical method for supercritical heat transfer of hydrocarbon fuels. Applied Physics Research, 2015, 7(1): 64–71.